Original Paper

Eletrônica de Potência
Open Journal of Power Electronics

Received July 31, 2025; Received in revised form November 02, 2025; Accepted November 11, 2025; Date of publication January 07, 2026.
The review of this paper was arranged by Associate Editor Francisco D. Freijedo and Editor-in-Chief Allan F. Cupertino.

Digital Object Identifier http://doi.org/10.18618/REP.e202602

Modeling and Control of a Full-Bridge DC-DC Converter for Arc Welding Applications

Christian G. Barbosa[1,3], **Vitor de S. Guedes**[1], **Rafael C. Beltrame**[1,*],
Lucas V. Bellinaso[1], **Fabio E. Bisogno**[2], **Ezequiel A. Mallmann**[3],
Luciano A. Fricke[3]

[1]Federal University of Santa Maria (UFSM), Power Electronics and Controle Research Group (GEPOC), Santa Maria – RS, Brazil.
[2]Ingenieurwesen Elektrotechnik und Informationstechnik Hochschule Koblenz, Koblenz, Germany.
[3]Fricke-Balmer Soldas Ltda, Ijuí – RS, Brazil.

e-mail: christian@fricke.com.br; vitor.guedes@acad.ufsm.br; beltrame@gepoc.ufsm.br*; lucas@gepoc.ufsm.br; bisogno@hs-koblenz.de;
mallmann@fricke.com.br; luciano@fricke.com.br.

*Corresponding author.

ABSTRACT This study presents the modeling and control of a full-bridge DC-DC converter applied to Gas Metal Arc Welding (GMAW) in short-circuit transfer mode. GMAW is widely used in industrial manufacturing due to its versatility. However, achieving stable operation in short-circuit transfer requires precise regulation of the welding current and arc voltage. To address this challenge, a simplified yet representative model of the converter and load dynamics is developed. Based on this model, a dual-loop digital control strategy is implemented to ensure fast transient response, reference tracking, and improved stability of the welding process. The effectiveness of the proposed approach is experimentally validated on an industrial-grade prototype, demonstrating agreement between theoretical predictions and measured waveforms.

KEYWORDS Arc welding, Converter modeling, Dual-loop control, GMAW modeling.

I. INTRODUCTION

Welding is a fundamental process in metal-mechanic industries, including areas such as aerospace and nuclear [1]. It can be defined as a method of joining materials in which the continuity of their chemical and physical properties is preserved. Currently, there are different welding processes, with electric arc-based methods being the most widely used. In these processes, the electric arc serves as the heat source to melt the base metal [2].

Electric arc welding processes can be further classified according to their application, with shielded metal arc welding (SMAW), metal inert/active gas welding (GMAW), and tungsten inert gas welding (GTAW) being the most common in the industry [1]. To meet the requirements of these different processes, each with distinct electrical and dynamic characteristics, modern welding machines employ power electronic converters capable of adapting their operating parameters accordingly [3–4].

Recent advances in welding power supplies have focused on replacing bulky low-frequency transformer-based sources with high-frequency switch-mode converters, which provide higher efficiency, faster dynamic response, and improved arc stability. For instance, [5] presents a comprehensive review of power-converter topologies and control strategies for welding applications, standing out the evolution from conventional 50/60 Hz transformer-rectifier units to high-frequency half-bridge, full-bridge and push-pull converters employing soft-switching techniques. In addition to hardware developments, modern control approaches – including predictive controllers, fuzzy-logic and classical dual-loop proportional-integral (PI) regulation – have been widely investigated to enhance the transient performance and arc stability of welding processes [6–8].

The choice of a static converter topology for welding equipment must consider several characteristics, such as high efficiency, the ability to supply high current, galvanic isolation, and a reduced number of active semiconductor switches and passive components. In this context, the phase-shifted full-bridge DC-DC converter meets these requirements, as it allows both high voltage gain and galvanic isolation through the use of a high-frequency transformer. Moreover, zero-voltage switching (ZVS) can be achieved using phase-shift pulse-width modulation (PS-PWM), which reduces switching losses and electromagnetic noise [9], as well as maximizing overall efficiency.

Dynamic modeling and control of the full-bridge DC-DC converter considering multiple welding processes is essential for the design of modern welding equipment's. The GTAW and SMAW processes require precise control of the current arc, whereas the GMAW process demands regulation of the average arc voltage, while simultaneously ensuring that the current does not exceed the converter's maximum allowable limit [10].

A common solution for controlling these processes involves a cascaded dual-loop controller: an inner current loop that calculates the phase-shift angle, used in all SMAW, GMAW and GTAW processes, and an outer average voltage loop that defines the current reference and is used just for the GMAW process [4].

One of the main challenges in control system design for this application is understanding and managing the complex dynamics of the welding process. Although the electrical circuits of the power converters used are relatively simple and widely discussed in the literature, incorporating models that represent the physical and electromechanical behavior of the welding arc introduces nonlinearity and time-variant characteristics to the system [10–11].

Among the three processes, GMAW has proven to be the most challenging from a modeling and control standpoint, particularly in the short-circuit transfer mode [1]. This is due to the frequent transitions between arc and short-circuit stages, which impose significant dynamic demands on the control system, requiring fast and precise responses to maintain process stability.

From the modeling perspective, small-signal models for phase-shifted full-bridge DC-DC converters available in the literature [12–14] typically establish the relationship between the phase angle and output voltage, assuming resistive or generic loads. These models neglect the highly time-varying behavior of the arc load. Therefore, this work presents a state-space average model of the phase-shifted full-bridge DC-DC converter considering a variable model for the arc and short phases, which is obtained through experimental waveforms.

This paper is an improved version of [15], and includes the following contributions:

- Development of a state-space model for the full-bridge isolated DC-DC converter supplying an arc load, including the modeling of the arc;
- Design of a digital dual-loop voltage and current controller for GMAW process using saturation and anti-windup logic to disable the outer average voltage loop when required;
- Experimental validation on an industrial-grade welding source prototype, demonstrating the response of controllers.

The paper is organized as follows: Section II derives the mathematical model of the converter and characterizes the arc load. Section III demonstrates the topology of the proposed converter. Section IV presents the small signal AC models. Section V presents the controller design, including saturation and anti-windup approaches. Section VI discusses the experimental results. Finally, Section VII presents conclusions and outlines directions for future work.

II. GMAW MODEL UNDER SHORT-CIRCUIT TRANSFER MODE

In the GMAW process operating in the short-circuit metal transfer mode, the metal deposition characteristic shows significant variations due to the alternating phases of arcing and short-circuiting [10]. As the wire is continuously fed toward the weld pool, the arc voltage tends to progressively decrease until a short-circuit occurs, characterized by direct contact between the wire and the molten pool.

The equipment used for GMAW typically features a constant (average) voltage output characteristic, which implies, as shown in Fig. 1, the availability of high current during short-circuit events. This high current is necessary to disrupt the contact between the wire and the weld pool, thereby re-establishing the electric arc. The process alternates between short-circuit periods, characterized by a significant ramp-up in current under reduced voltage, and arc periods, marked by a decrease in current and an increase in voltage drop. In this figure, $v_{w,min\ k}$ and $v_{w,max\ k}$ denote the minimum and maximum arc voltages, respectively, while $i_{w,min}$ and $i_{w,max}$ represent the minimum and maximum current levels during each stage k.

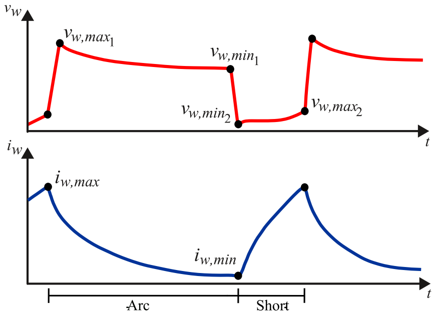

FIGURE 1. Theoretical voltage and current during short-circuit metal transfer [18].

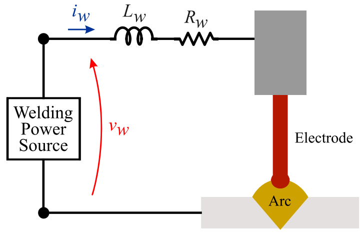

FIGURE 2. Simplified diagram for the short-circuit GMAW process

Technical literature presents a wide range of studies aimed at modeling this mode of metal transfer. Dynamic models are presented in [10–11] and [16–18]. Other studies propose hybrid system approaches that divide the process into two distinct phases, allowing the equations describing the physical phenomena involved in the short-circuit and arc phases to alternate consecutively [19]. More simplified models perform the analysis based on the characteristic waveforms of the process to derive the model [20].

In this study, a more simplified approach was adopted with the aim of enabling, in later stages, the integrated modeling of the power converter with the welding process. Accordingly, the short-circuit GMAW process can be electrically represented by the simplified diagram shown in Fig. 2. In this model, L_W represents the equivalent inductance of the welding cables and connections, while R_W denotes the equivalent resistance of the conductors, the electrode and the arc. The voltage source V_T, although not explicitly illustrated in Fig 2, is included in the mathematical model as a lumped parameter that represents the combined voltage drops across the arc column, the stick-out region of the wire, and the molten metal bridge that forms short-circuit events. The relationship that describes the model, where v_W represents the welding process voltage, is expressed as:

$$v_W = R_W i_W + L_W\, \mathrm{d}i_W/\mathrm{dt} + V_T. \qquad (1)$$

The inductance L_W depends on external factors such as the cable arrangement in the application (e.g., coiled or laid out straight) [21], inductances associated with the connections, and the specific cable model used in the equipment. This way, it is recommended to measure L_W for a specific application.

In [19], the voltage V_T is described separately for each phase. During the short-circuit phase, V_T is given by the sum of the constant short-circuit voltage (V_{sh0}), the stick-out

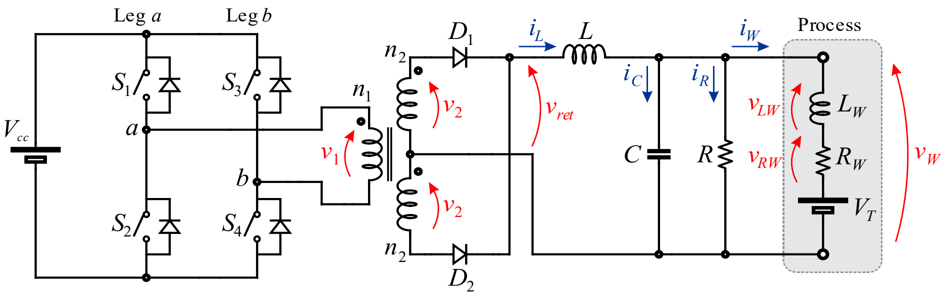

FIGURE 3. Full-bridge DC-DC converter circuit and load model [15].

voltage (V_e) and the bridge voltage (V_b). In the arc phase, V_T corresponds to the sum of the arc voltage (V_a) and the stick-out voltage:

$$V_T = \begin{cases} V_{sho} + V_e + V_b \text{ , for short} - \text{circuit} \\ V_a + V_e \text{ , for arc} \end{cases} . \tag{2}$$

Although this model provides a more detailed representation of the process, its integration with the power converter can become complex due to the high variability in droplet characteristics and arc geometry, which directly affect the values of V_T over time.

Still based on the two stages analysis approach and on the study presented in [20], which proposed a control based on a representative waveform, the parameters R_W and V_T can be determined by assuming an approximately linear relationship between voltage and current during each phase of the welding.

The characteristic waveform shown in Fig. 1 was constructed as a representative short-circuit metal transfer profile, combining the theoretical behavior of the process with sampled experimental data acquired from industrial-grade welding power sources exhibiting comparable dynamic performance. An example of the measured waveforms, recorded during the experimental validation of this study, is presented in Fig. 17. So, the relationship is given by $v_W = R_W \cdot i_W + V_T$, which disregards the impact of L_W and offers a simple and effective analytical basis that can be applied directly to experimental data, where the minimum and maximum levels defined in Fig. 1 are used for both the short-circuit and arc intervals. Thus, based on Fig. 1, it is straightforward to demonstrate that

$$R_{W_k} = \frac{v_{W,max_k} - v_{W,min_k}}{i_{W,max} - i_{W,min}} , \tag{3}$$

$$V_{T_k} = v_{W,min_k} - \left(\frac{v_{W,max_k} - v_{W,min_k}}{i_{W,max} - i_{W,min}} \right) i_{W,min} , \tag{4}$$

where k represents the welding stage, with $k = 1$ for the arc stage and $k = 2$ for the short-circuit one.

III. PHASE-SHIFTED FULL-BRIDGE DC-DC CONVERTER

The full-bridge DC-DC converter topology employed in this application is shown in Fig. 3, including the elements that compose the welding process model, represented by R_W, L_W and V_T. In this figure, V_{cc} is DC bus voltage, S_1 to S_4 are the semiconductor switches, D_1 and D_2 are the rectifier diodes, R, L and C are the output filter resistor, inductor and capacitor, respectively, and n_1 and n_2 are the number of turns of the primary and secondary windings. It is worth noting that the transformer leakage inductance and the intrinsic capacitances of the semiconductor switches S_1 to S_4 are not considered.

The switching control is based on the phase-shift PWM modulation strategy. This approach offers the advantage of applying zero average voltage across the transformer, thus avoiding magnetic core saturation, and enables ZVS for the semiconductor switches S_1 to S_4 by allowing the transformer's leakage inductance to resonate with the intrinsic capacitances of these switches.

In the typical implementation of this strategy, the semiconductor switches of both converter legs *a* and *b* operate with a fixed duty cycle of 0.5, but with their carrier signals phase-shifted by an angle φ. That is, switches S_1 and S_2 of leg *a* ideally operate in a complementary manner, each conducting for half of the switching period T_S. The same applies to S_3 and S_4 of leg *b*, but the gating signals of S_1 and S_3 are phase-shifted. The RMS voltage applied to the transformer primary (v_1) reaches its maximum value when the carrier signals are phase-shifted by 180°, and it decreases as the phase-shift is reduced.

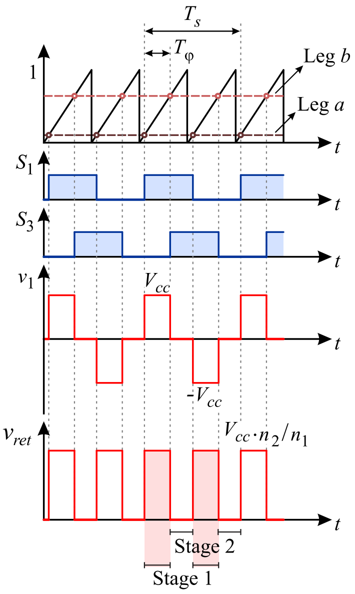

FIGURE 4. Main waveforms of the phase-shift PWM modulation strategy [15].

It should be emphasized that the relationship between the phase shift angle φ and v_1 (and, consequently, its effect on the welding process variables) may vary depending on how the PS-PWM is implemented in the microcontroller selected for the application. For instance, the method illustrated in Fig. 4, which uses a single sawtooth carrier with twice the switching frequency, is compatible with the STM32F446xx microcontroller [22]. The gating signals for switches S_1 (leg *a*) and S_3 (leg *b*) undergo a logical level toggle each time the rising edge of the sawtooth carrier reaches the comparison level of the corresponding leg (output compare mode). Thus, it is possible to vary the phase-shift between the PWM signals of legs a and b simply by adjusting the respective comparison levels of each leg relative to the sawtooth waveform.

For the implementation of the PS-PWM shown in Fig. 4, the relationship between the effective duty-cycle and the phase-shift angle is given by:

$$D = \frac{\varphi}{180^\circ}, \tag{5}$$

where, $D = 2T_\varphi / T_S$, with $T_\varphi = [0 \quad T_S/2]$.

Although the control variable of the converter is the phase-shift angle φ of the modulation, the following modeling approach employs the concept of effective duty-cycle [23], that is, the equivalent pulse-width of a conventional PWM signal that results in the same average voltage after the converter's rectifier stage (v_{ret}). Accordingly, the derivation of the state-space model describing the behavior of the converter's variables of interest can follow the procedure outlined in [24].

IV. SMALL-SIGNAL AC MODELS

In the following analysis, the resonant stages between the transformer leakage inductance and the switch capacitances are disregarded. In practice, these stages occur during the dead-time interval between the commutation of complementary switches in each leg. A detailed analysis of the operation of the full-bridge DC-DC converter with phase-shift PWM can be found in [23].

As shown in Fig. 4, the converter operates in four stages, namely: (i) S_1 and S_4 active, (ii) S_1 and S_3 active, (iii) S_2 and S_3 active, and (iv) S_2 and S_4 active. It can be observed that in stages (i) and (iii), the DC bus voltage is applied to the primary of the transformer ($v_1 = \pm V_{cc}$), enabling energy transfer to the secondary side. On the other hand, during stages (ii) and (iv), a freewheeling interval occurs, in which v_1 is zero. It is worth noting that stages (iii) and (iv) are complementary to (i) and (ii), and, therefore, they will not be analyzed.

Furthermore, it is assumed that the resonance period of the transformer leakage inductance (L_R) with the drain-source capacitances (C_1 to C_4) of the semiconductor switches is much shorter than T_S, and can be neglected. The equivalent series resistance (ESR) of the inductors and capacitors is also neglected. Basically, L_R and ESR maximize the damping factor of the small-signal AC model [12]. Therefore, the model derived in this work represents a conservative approach, since a model with a lower damping factor tends to make the control system design more challenging.

A. STATE-SPACE MODEL

Stage 1: $0 \le t < d(t)T_S$

The converter configuration during this stage is shown in Fig. 5 (a). The time duration of this stage is defined as $d(t)T_S$, where $d(t)$ is the effective duty-cycle of the converter, which varies over time.In this stage, the equations governing the behavior of the filter inductor current (i_L), the welding process current (i_W), and the welding process voltage (v_W) are given, respectively, by:

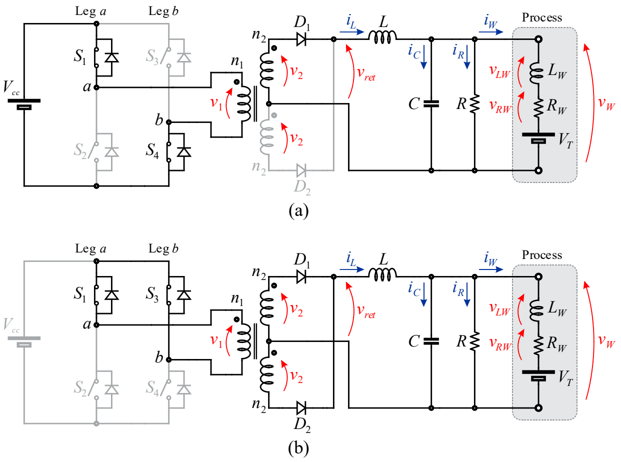

FIGURE 5. Converter operating stages. (a) Stage 1 (energy transfer). (b) Stage 2 (freewheeling) [15].

$$\begin{aligned} L\frac{\mathrm{d}i_L(t)}{\mathrm{d}t} &= -v_W(t) + \frac{V_{cc}}{n}, \\ L_W\frac{\mathrm{d}i_W(t)}{\mathrm{d}t} &= -i_W(t)R_W + v_W(t) - V_T\,, \\ C\frac{\mathrm{d}v_W(t)}{\mathrm{d}t} &= i_L(t) - i_W(t) - \frac{v_W(t)}{R}. \end{aligned} \tag{6}$$

In the previous equation, n is the transformer turns ratio, defined as $n = n_1/n_2$.

Stage 2: $d(t)T_S \le t < T_S$

For this stage, the converter configuration is shown in Fig. 5 (b), and its time duration is $T_S - d(t)T_S$. The filter inductor current (i_L), the welding process current (i_W), and the welding process voltage (v_W) are given, respectively, by:

$$\begin{aligned} L\frac{\mathrm{d}i_L(t)}{\mathrm{d}t} &= -v_W(t)\,, \\ L_W\frac{\mathrm{d}i_W(t)}{\mathrm{d}t} &= -i_W(t)R_W + v_W(t) - V_T\,, \\ C\frac{\mathrm{d}v_W(t)}{\mathrm{d}t} &= i_L(t) - i_W(t) - \frac{v_W(t)}{R}. \end{aligned} \tag{7}$$

It is noted that, in both analyzed stages, switch S_1 remains turned-on. In the two complementary stages (whose analysis can be omitted without loss of generality), switch S_2 would remain turned-on. Further details can be found in [15].

B. SMALL-SIGNAL AC MODEL FOR THE CURRENT LOOP

The primary objective of the converter's control system is to regulate the welding process current (i_W), regardless of which welding process is being used (SMAW, GMAW or GTAW). In this case, the control action is the effective duty-cycle (actually, the phase shift angle φ).

Thus, as presented in [23], the state equations of the small-signal AC model are expressed in (8)-(9), where $\hat{\mathbf{u}}_\mathrm{p}(t) = [\hat{\mathbf{u}}(t) \quad \hat{d}(t)]^T = [\hat{v}_{cc}(t) \quad \hat{v}_T(t) \quad \hat{d}(t)]^T$. It is important to note that $\hat{\mathbf{u}}(t)$ and $\hat{d}(t)$ represent small AC perturbations in the input vector and in the effective duty-cycle, respectively, while $\hat{\mathbf{x}}(t) = [\hat{\imath}_L(t) \quad \hat{\imath}_W(t) \quad \hat{v}_W(t)]^T$ and $\hat{y}(t) = [\hat{\imath}_W(t)]$ represent the resulting AC variations in the state vector and the output variable, respectively.

$$\frac{\mathrm{d}\hat{\mathbf{x}}(t)}{\mathrm{d}t} = \mathbf{A_p}\hat{\mathbf{x}}(t) + \mathbf{B_p}\hat{\mathbf{u}}_\mathbf{p}(t)\,, \qquad (8)$$
$$\hat{y}(t) = \mathbf{H_p}\hat{\mathbf{x}}(t) + \mathbf{E_p}\hat{\mathbf{u}}_\mathbf{p}(t)\,,$$

where:

$$\mathbf{A_p} = \begin{bmatrix} 0 & 0 & -\frac{1}{L} \\ 0 & -\frac{R_W}{L_W} & \frac{1}{L_W} \\ \frac{1}{C} & -\frac{1}{C} & -\frac{1}{RC} \end{bmatrix},$$
$$\mathbf{B_p} = \begin{bmatrix} \frac{D}{nL} & 0 & \frac{V_{cc}}{nL} \\ 0 & -\frac{1}{L_W} & 0 \\ 0 & 0 & 0 \end{bmatrix}, \qquad (9)$$
$$\mathbf{H_p} = [0 \quad 1 \quad 0] \text{ and } \mathbf{E_p} = [0 \quad 0 \quad 0]\,.$$

The transfer functions relating the output variable of the model to the input variables can be obtained by applying the Laplace Transform to (8), resulting in:

$$\hat{y}(s) = \mathbf{H_p}\left(s\mathbf{I_{3,3}} - \mathbf{A_p}\right)^{-1}\mathbf{B_p}\hat{\mathbf{u}}_\mathbf{p}(s)\,. \qquad (10)$$

In this case, since the interest lies solely in the relationship between the welding process current $\hat{\imath}_W(t)$ and the effective duty-cycle $\hat{d}(t)$, it is defined that $\hat{v}_{cc}(t) = 0$ and $\hat{v}_T(t) = 0$. Then, by solving (10) and considering that $\hat{d}(s) = \hat{\varphi}(s)/180°$ (obtained from the perturbation and linearization of (5), it is possible to show that:

$$G_{iW,\varphi}(s) \triangleq \frac{\hat{\imath}_W(s)}{\hat{\varphi}(s)} = \frac{1}{180}\,\frac{V_{cc}/n}{b_1 s^3 + b_2 s^2 + b_3 s + b_4}, \qquad (11)$$

where:

$$b_1 = CLL_W\,, \qquad b_2 = L\left(CR_W + \frac{L_W}{R}\right),$$
$$b_3 = L_W + L + \frac{LR_W}{R} \text{ and } b_4 = R_W\,. \qquad (12)$$

C. SMALL-SIGNAL AC MODEL FOR THE VOLTAGE LOOP

Assuming the current loop controller is properly designed, $i_W(t)$ can be represented as a current source for the voltage loop, as shown in Fig. 6, provided that the voltage loop bandwidth is significantly lower than the current loop bandwidth (e.g., one decade lower). So, the welding process voltage is then given by:

$$v_W(t) = v_{LW}(t) + v_{RW}(t) + V_T\,, \qquad (13)$$

where $v_{LW}(t)$ is the voltage drop across the inductance associated with the cable connecting the machine output to the electrode, and $v_{RW}(t)$ is the voltage drop across the resistances of the cable, the electrode and the arc. The voltage V_T has been previously defined as dependent of the arc or short-circuit phase.

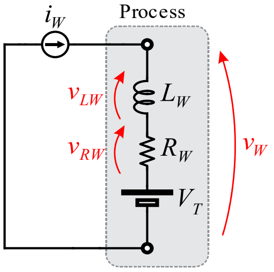

FIGURE 6. Equivalent circuit for the small-signal AC model of the process [15].

With respect to the circuit in Fig. 6, it is identified that $v_{LW}(t) = L_W\,\mathrm{d}i_W(t)/\mathrm{d}t$ and $v_{RW}(t) = R_W i_W(t)$. These relations can thus be substituted into (13). In order to derive the linear small-signal AC model, all variables are considered to be composed of their steady-state value plus a small AC perturbation, that is: $v_W(t) = \bar{V}_W + \hat{v}_W(t)$, $i_W(t) = \bar{I}_W + \hat{\imath}_W(t)$ and $V_T(t) = \bar{V}_T + \hat{v}_T$. Substituting these expressions into (13), disregarding the DC terms and applying the Laplace Transform, the small-signal AC model is obtained, assuming the perturbation $\hat{v}_T(t) = 0$:

$$G_{vW,iW}(s) \triangleq \frac{\hat{v}_W(s)}{\hat{\imath}_W(s)} = L_W\left(s + \frac{R_W}{L_W}\right). \qquad (14)$$

V. PROPOSED DUAL-LOOP CONTROL

The control diagram proposed for the GMAW process is shown in Fig. 7. It consists of two control loops, an inner (fast) loop that regulates the welding current i_W, and an outer (slow) loop responsible for controlling the welding voltage v_W. As illustrated in Fig. 7, the current control loop operates with two reference signals, $i_{W,ref}$ and $i_{W,base}$. The reference $i_{W,ref}$ is generated by the outer voltage control loop and can be disabled (set to zero) when the voltage regulation is not required, such as in the SMAW and GTAW process.

On the other hand, the $i_{W,base}$ can be used in combination with $i_{W,ref}$ to establish a minimum baseline current for the GMAW process. Alternatively, it can serve as the sole reference in welding processes that utilize only single current control loop, as it is typical in SMAW and GTAW applications.

Furthermore, a saturation block is applied to limit the phase angle φ used in the modulation, ensuring it remains within its theoretical operational bounds, typically between 0° (φ_{min}) and 180° (φ_{max}). To maintain control performance under saturation conditions, an anti-windup strategy is integrated into the current control loop. This mechanism prevents integrator windup and mitigates overshoot in scenarios where the control effort exceeds the permissible range, specifically, when $\varphi < \varphi_{min}$ or $\varphi > \varphi_{max}$.

In the outer control loop responsible for regulating the arc voltage, also depicted in Fig. 7, the reference signal $v_{W,ref}$ corresponds to the voltage setpoint defined by the operator through the human machine interface (HMI) of the welding equipment. This reference serves as the desired average arc voltage level to be regulated during the welding process, guiding the overall regulation strategy implemented in the control system.

To enable compatibility with other welding processes such as SMAW and GTAW, the voltage reference $v_{W,ref}$ can be intentionally set to -1, as determined by the control flag $C_{v,enable}$. In this condition, since negative arc voltages are physically unfeasible, due to the unidirectional nature of the

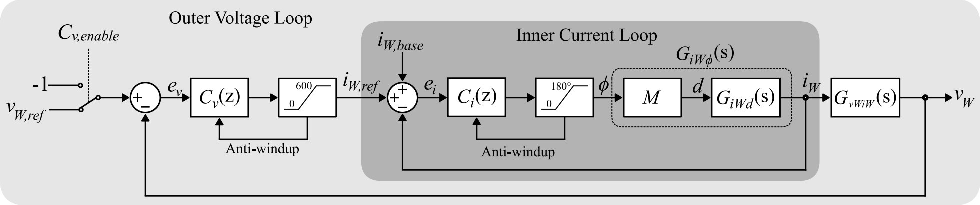

FIGURE 7. Proposed dual-loop control approach.

employed DC-DC converter topology, the saturator located at the output of the voltage loop controller limits the control action to zero, effectively forcing $i_{W,ref} = 0$, disabling this control loop. Additionally, an anti-windup strategy is carefully incorporated into the voltage control loop to prevent integrator windup and reduce overshoot in scenarios where $i_{W,ref} < 0$ A or $i_{W,ref} > 600$ A (for this application).

TABLE 1. Control system specifications.

Parameter	Description	Specification
f_{ai}	Sampling frequency of the current control loop	80 kHz
f_{ci}	Crossover frequency of the current control loop	2 to 4 kHz
MF_i	Minimum phase margin for the current control loop	60°
f_{av}	Sampling frequency of the voltage control loop	80 kHz
f_{cv}	Crossover frequency of the voltage control loop	100 to 400 Hz
MF_v	Minimum phase margin for the voltage control loop	60°

TABLE 2. Converter parameters.

Parameter	Description	Specification
i_W	Process current (steady-state)	10 to 300 A
f_s	Switching frequency	40 kHz
V_{cc}/n	Open-circuit voltage	68 to 78 V
n_1/n_2	Turns ratio	8/2 = 4
L_m	Transformer magnetizing inductance (primary side)	800 μH
L_R	Transformer leakage inductance (reflected to primary side)	5.7 μH
Core	Transformer core (ferrite type)	2 × EE85/43/26
L	Filter inductance	15 μH
C	Filter capacitance	5 nF
R	Filter resistance	Not used
$L_W{}^{(1)}$	Process inductance	3 to 7 µH
$R_W{}^{(1)}$	Process resistance (arc stage)	55 mΩ
	Process resistance (short stage)	25 mΩ
$V_T{}^{(1)}$	Arc voltage (arc stage)	14.45 V
	Arc voltage (short stage)	1.12 V

(1) L_W, R_W and V_T were obtained experimentally as described in Section II.

It is important to emphasize that the gains associated with the sensing of current and voltage signals are assumed to be unitary, as the required scaling is implemented directly in the firmware of the STM32F446xx microcontroller. Moreover, the dynamics introduced by signal conditioning filters, such as anti-aliasing filters, are neglected in the control design, given that their cutoff frequencies are significantly higher than the crossover frequencies employed in the control loops, thus having negligible impact on the system's dynamic behavior.

The main control specifications adopted for the design of the current and voltage controllers are summarized in Table 1. These include the sampling frequencies (f_{ai}, f_{av}), crossover frequencies (f_{ci}, f_{cv}), and minimum phase margin requirements (MF_i, MF_v) for both loops. Such parameters were selected to ensure fast dynamic response, adequate stability margins, and compatibility with the digital implementation constraints of the low-cost STM32F446xx microcontroller.

A. CURRENT LOOP CONTROLLER

Considering the specifications and parametric variations outlined in Table 2, the corresponding Bode plots derived from (11) are presented in Fig 8. The analyzed frequency range spans from 10 Hz to 100 kHz, which is appropriate for assessing the system's behavior around the target crossover region. Notably, the uncompensated current control loop naturally presents a crossover around one decade below the sampling frequency, with value varying according to the plant parameters in Table 2.

An examination of Fig. 8 shows that variations in the cable inductance L_W mainly shift the dominant pole to lower frequencies, leading to an earlier roll-off and increased phase lag near the desired crossover frequency. Changes in the equivalent resistance R_W reduces the low-frequency gain with minor effect on phase, while adjustments in V_{cc}/n mainly scale the magnitude response without changing pole locations.

As illustrated in Fig. 8, all transfer functions exhibit qualitatively similar frequency responses. Among the various parameter combinations, "Combination #7" presents an intermediate gain profile, and a slightly steeper phase fall compared to the others. Therefore, this configuration (corresponding to V_{cc}/n = 78 V, L_W = 7 µH and R_W = 25 mΩ) is selected as the representative case for design of the current control loop. Apart from that, the stability of the loop will be confirmed for all remaining combinations.

For this control loop, a PI controller is proposed. The controller's pole is placed at the origin, while the zero is positioned at approximately 400 Hz to preserve the desired phase margin of the system. Nevertheless, the design specifications in Table 1 establish a target range for the crossover frequency of 2–4 kHz for the compensated loop, considering the worst-case plant scenario, which is achieved after tuning the PI controller.

The resulting compensated open-loop frequency response is shown in Fig. 9. The achieved phase margin was 73º for a crossover frequency of 2 kHz. In addition, the stability of the closed-loop system was further verified through the continuous-time root locus shown in Fig. 10. The plot confirms that all closed-loop poles are in the left-hand half of the s-plane, even under the parameter variations (V_{cc}/n, R_W and L_W) summarized in Table 2. This result demonstrates that the designed controller ensures closed-loop stability for all operation conditions.

B. VOLTAGE LOOP CONTROLLER

Considering once again the parametric variations presented in Table 2, the Bode plots corresponding to (14) are shown in Fig. 11, covering the frequency range from 10 Hz to 100 kHz. Each curve corresponds to a different pair (R_W,

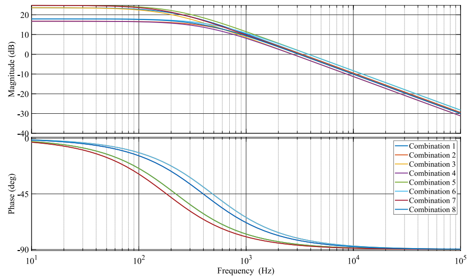

FIGURE 8. Bode plots of the transfer function $G_{iW,\varphi}(s)$.

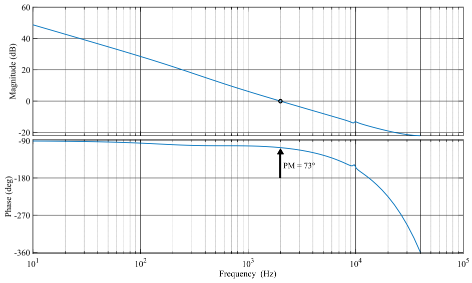

FIGURE 9. Bode plot of the compensated open-loop transfer function for the current loop.

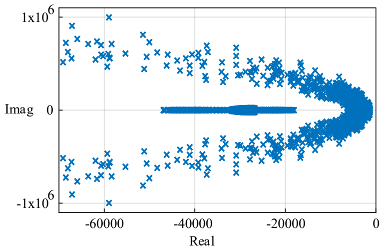

FIGURE 10. Closed-loop pole locations under parametric variations for the current loop.

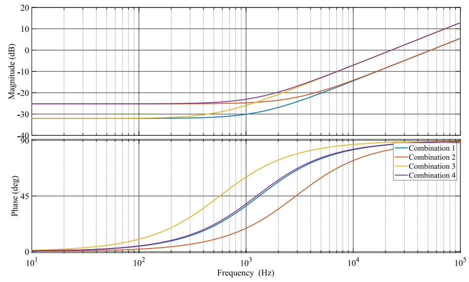

FIGURE 11. Bode plots of the transfer function $G_{vW,iW}(s)$.

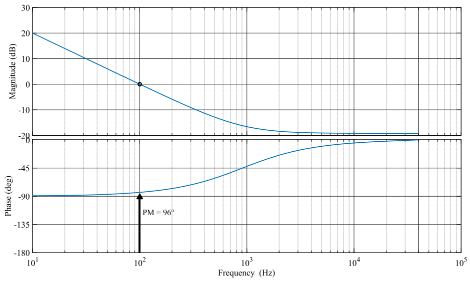

FIGURE 12. Bode plot of the compensated open-loop transfer function for the voltage loop.

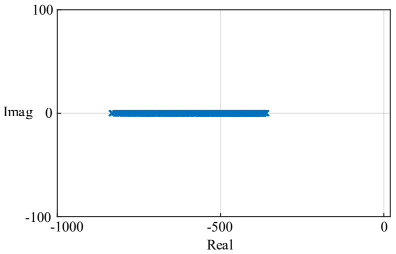

FIGURE 13. Closed-loop pole locations under parametric variations for the voltage loop.

L_W), while V_T is kept constant since it does not appear in (14). Increasing R_W raises the low-frequency gain and shifts the corner frequency $\omega_z = R_W/L_W$ to higher values, whereas increasing L_W moves this corner to lower frequencies.

As observed in Fig. 11, all four transfer functions exhibit qualitatively similar behavior. “Combination #2” presents a slightly higher gain and a slightly lower phase within the frequency range of interest. Therefore, this configuration (defined by L_W = 7 μH and R_W = 25 mΩ) is selected for the design of the voltage control loop. It is worth noting that these are the same parameters previously adopted for the design of the process current control loop, ensuring consistency in the modeling assumptions and controller design approach. Further, the value of V_T has no impact on the dynamics of both loops.

For the voltage control loop, an integral-type (I) controller is proposed, with its pole placed at the origin to ensure zero steady-state error for a voltage step reference. The desired crossover frequency was defined as f_{cv} = 100 Hz, in accordance with the specifications outlined in Table 1. The resulting compensated open-loop frequency response is shown in Fig. 12. The achieved phase margin was 96º. The plot in Fig. 13 confirms that all closed-loop poles remain in the left-hand side of the s-plane for the entire range of parameter variations summarized in Table 2, proving that the voltage control loop also preserves stability under the expected operating conditions.

VI. EXPERIMENTAL RESULTS

To validate the effectiveness of the proposed modeling approach and the implemented control system, this section presents experimental results obtained from an industrial-grade prototype with the main specifications summarized in Table 2. The implemented converter is shown in Fig 14. The inverter stage employs Silan IGBT modules rated at 1200 V and 120 A, suitable for high-current welding applications, since with the current transformer turns ratio, the nominal current through the switches is approximately 75 A. The rectifier stage is composed of Vishay discrete ultrafast recovery diodes rated at 400 V and 60A connected in parallel, ensuring low reverse recovery and reliable operation under the high current ripple conditions.

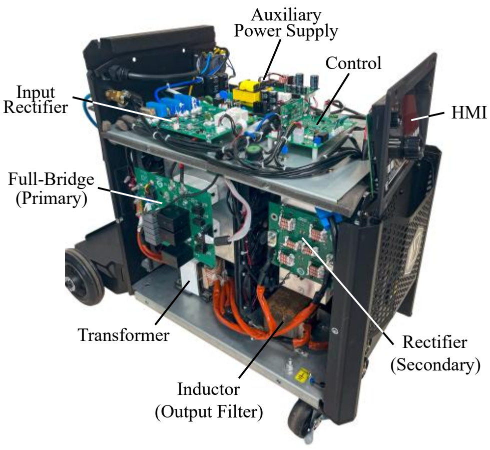

FIGURE 14. Implemented converter prototype.

The system response to a step change in the current reference (from 60 A to 100 A) is illustrated in Fig. 15 (for a fixed load). As observed, the digital control system, designed

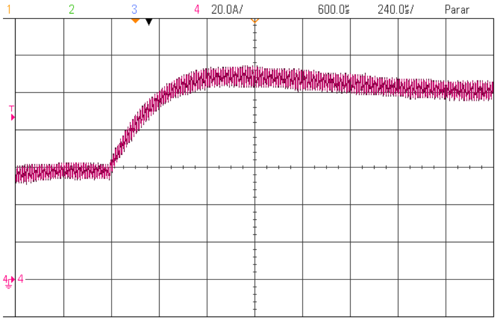

FIGURE 15. Process current control loop: step response.

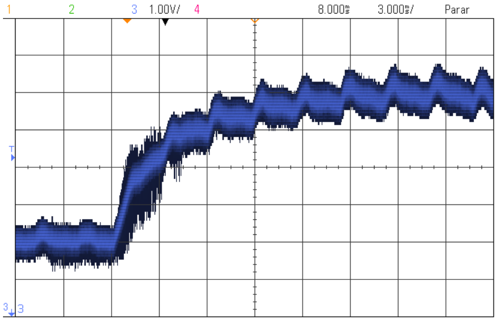

FIGURE 16. Process voltage control loop: step response.

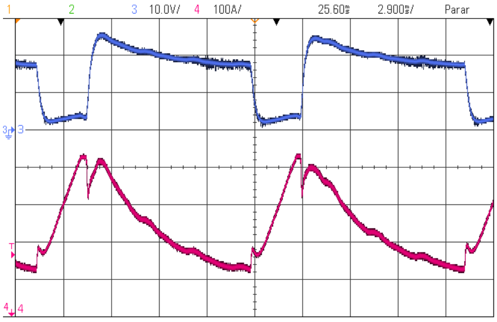

FIGURE 17. Process voltage control loop: Rejection of process disturbances.

FIGURE 18. Welding using a prototype with different set-points: (a) 18 V – 5.0 m/min, (b) 16 V – 4.5 m/min, and (c) 14 V – 3.5

based on the developed converter model, successfully ensures accurate tracking of the current reference with zero steady-state error. An overshoot of about 10% and a settling time of 600 µs were observed, both of which are considered appropriate for this kind of application. Additionally, a high-frequency ripple superimposed on the current waveform can be seen, which is attributed to the switching nature of the converter. This behavior is consistent with the expected operation and does not compromise the overall performance of the current regulation loop.

The system response to a step change in the voltage reference (from 14 V to 18 V) is illustrated (for a fixed load) in Fig. 16. It should be noted that this test considers both the current and voltage control loops operating in a closed-loop configuration. As shown, the proposed digital control system is capable of accurately tracking the reference voltage (actually, its average value), ensuring a satisfactory dynamic response (no overshoot and a settling time of about 15 ms).

A periodic ripple is observed superimposed on the voltage waveform in both operating regions. This oscillation originates from the DC-link voltage ripple, which is inherently related to the rectified input voltage from the AC mains, typically at twice the grid frequency (120 Hz for single phase in this case). Although this ripple could be simple rejected through an additional control action, such strategy is beyond the scope of this work. The primary objective here is to validate the proposed modeling approach and the effectiveness of the implemented control structure under realistic operating conditions, including the influence of bus voltage oscillations.

Fig. 17 presents the dynamic behavior of both the process voltage (upper waveform, in blue) and process current (lower waveform, in pink), considering a voltage reference set to 16 V (this value is typically configured by the operator through HMI of the equipment), in a real welding condition. In this experiment, the parameters R_W and V_T are varied from 55 mΩ and 14.45 V (characterizing arcing conditions) to 25 mΩ and 1.12 V (representing short-circuit conditions). As observed, the voltage drops momentarily due to the severe and abrupt change in the load characteristics, leading to an increase in current. Nonetheless, the control system responds effectively, and the process variables return to their expected operating levels.

The weld beads obtained under three different set points, using a 1.0 mm wire and mixed shielding gas, are shown in Fig. 18. A mechanized torch support was used to ensure constant travel speed and stick-out, thus minimizing external disturbances and enabling a fair comparison between conditions. The resulting beads exhibit satisfactory performance, with good geometric uniformity along the entire length and visibly low spatter formation, demonstrating the stability of the arc and the consistent control achieved by the proposed system across the tested operating points.

VII. CONCLUSION

The obtained results reinforce the validity of the proposed modeling approach, which integrates the power converter with the nonlinear behavior of the GMAW load. This work advances the modeling previously presented in [15] where based on this model, the control strategy was designed to handle fast process variations, ensuring system stability, accurate reference tracking and consistent regulation.

Furthermore, the voltage and current waveforms obtained experimentally in Fig. 17 closely resemble the theoretical profiles presented in Fig. 1, which characterize the short-circuit metal transfer mode in GMAW. This experimental validation demonstrates the effectiveness of the proposed digital dual-loop controller with saturation and anti-windup strategy in a real welding prototype.

It is worth noting that classical PI/PID controllers may experience performance degradation when the actuator saturates and the current reference crosses near zero, leading to slower recovery and minor transient distortions during short-circuit events [25]. In this work, these effects were mitigated by incorporating anti-windup strategy and current-reference limiting in the inner loop (Fig. 7). Although slight nonlinearities can still be observed in Fig. 17, they do not compromise the objectives achieved. Acknowledging this limitation, however, highlights opportunities for further refinement of the control scheme.

In particular, the agreement between theoretical and experimental results further validates the accuracy of the proposed converter-load model and confirms its capability to reproduce the intrinsic dynamics of the welding process under realistic operating conditions.

Future research could explore additional nonlinear characteristics of the welding process, such as the dynamic behavior of metal transfer and variations in wire feeding speed. Moreover, implementing adaptive or predictive control strategies based on the developed model may enhance system performance under diverse operating conditions. Experimental validation in a broader range of welding scenarios, including different materials and shielding gases, would also contribute to generalizing the applicability of the proposed approach.

ACKNOWLEDGMENT

The authors are grateful for the financial support provided through the R&D partnership agreement n. CTTPI026/2023, established between the Federal University of Santa Maria (UFSM) and Fricke–Balmer Soldas Ltda, and CNPq process n. 312046/2025-1.

AUTHOR’S CONTRIBUTIONS

C.G.BARBOSA: Data Curation, Investigation, Methodology, Software, Validation, Writing – Original Draft, Writing – Review & Editing. **V.S.GUEDES:** Software, Validation, Writing – Original Draft, Writing – Review & Editing. **R.C.BELTRAME:** Conceptualization, Formal Analysis, Funding Acquisition, Investigation, Methodology, Project Administration, Software, Supervision, Validation, Writing – Original Draft, Writing – Review & Editing. **L.V.BELLINASO:** Conceptualization, Formal Analysis, Investigation, Methodology, Resources, Writing – Review & Editing. **F.E.BISOGNO:** Conceptualization, Funding Acquisition, Methodology, Resources, Writing – Review & Editing. **E.A.MALLMANN:** Writing – Review & Editing. **L.A.FRICKE:** Writing – Review & Editing.

PLAGIARISM POLICY

This article was submitted to the similarity system provided by Crossref and powered by iThenticate – Similarity Check.

DATA AVAILABILITY

The data used in this research is available in the body of the document.

REFERENCES

[1] L. Jeffus, “Welding: Principles and Applications,” 8th ed. Boston, MA, USA: Cengage Learning, Aug. 2016, ISBN: 978-1305494695.

[2] R. Singh, “Arc Welding Processes Handbook,” Beverly, MA, USA: Scrivener Publishing, Oct. 2021, ISBN: 978-1-119-81905-9.

[3] N. Blasco, A. Martinez, F. J. P. Cebolla, J. E. Vicuna, I. Lacamara and J. A. Oliva, “Evaluation of power converters for MMA arc welding,” in *Proc. IEEE International Symposium on Industrial Electronics*, pp. 365-370, Jun. 2007, doi: 10.1109/ISIE.2007.4374625.

[4] S. A. Vendan, L. Gao, A. Garg, P. Kavitha, G. Dhivyasri and S. Rahul, “Interdisciplinary Treatment to Arc Welding Power Sources,” Singapore: Springer, Jan. 2019, doi: 10.1007/978-981-13-0806-2.

[5] I. Hassan, K. Sayed, M. D. Alanazi, H. A. Ziedan and M. Abdelsattar, “A comprehensive review of power converter topologies and control techniques for welding power supply applications,” *Discover Applied Sciences*, vol. 7, Sep. 2025, doi: 10.1007/s42452-025-07180-1.

[6] P. Hu, J. Huang and M. Zeng, “Application of fuzzy control method in gas metal arc welding,” *International Journal of Advanced Manufacturing Technology*, vol. 92, pp. 1769-1775, Mar. 2017, doi: 10.1007/s00170-017-0245-x.

[7] C. Dong, J. Xue and Y. Hu, “Control study of pulsed MIG high-speed welding power source based on single neuron adaptive PID model,” in *Proc. International Conference on Intelligent Human-Machine Systems and Cybernetics*, pp. 381-385, 2018, doi: 10.1109/IHMSC.2018.10192.

[8] S. Chaouch, S. Kahla, B. Babes, N. Hamouda, A. Boutaghane and M. Hasni, “PSFB DC-DC LCLC resonant converter voltage and current modes control using Arduino-Mega,” in *Proc. International Conference on Electronics, Energy and Measurement*, pp. 1-6, 2023, doi: 10.1109/IC2EM59347.2023.10419417.

[9] A. U. Lappeenrantaensis, “Performance and scalability of isolated DC-DC converter topologies in low voltage, high current applications,” Ph.D. thesis, Lappeenranta University of Technology, Lappeenranta, Finland, 2012. ISBN: 978-952-265-351-2.

[10] S. Ozcelik and K. Moore, “Modeling, sensing and control of gas metal arc welding,” Oxford: Elsevier, Jun. 2003. ISBN: 978-0-08-044066-8.

[11] P. J. D. O. Evald, J. L. Mór, R. Z. Azzolin and S. S. C. Botelho, “A nonlinear coupled-variables model for mass transfer modes in MIG-MAG processes with experimental validation,” *International Journal of Modelling, Identification and Control*, vol. 31, no. 4, p. 361-373, Jan. 2019, doi: 10.1504/IJMIC.2019.099813.

[12] V. Vlatkovic, J. A. Sabate, R. B. Radley, F. C. Lee, and B. H. Cho, “Small-signal analysis of the phase-shifted PWM converter,” IEEE Transactions on Power Electronics, vol. 7, no. 1, pp. 128-135, Jan. 1992, doi: 10.1109/63.124585.

[13] C. Zanatta and J. R. Pinheiro, “A no dc-gain error small-signal model for the zero-voltage-switching phase-shift-modulated full-bridge dc-dc converter,” in *Proc. IEEE Annual Conference on IEEE Industrial Electronics*, pp. 1921-1926, 2006, doi: 10.1109/IECON.2006.348128.

[14] H. Xuezhi, and N. Guangqun, “The research of modeling and simulation for phase-shifted full-bridge ZVS dc/dc converter,” in *Proc. IEEE International Symposium on Intellgent Information Technology Application*, pp. 550-553, Nov. 2009, doi: 10.1109/IITA.2009.185.

[15] V. S. Guedes, F. E. Bisogno, L. V. Bellinaso, R. C. Beltrame, C. G. Barbosa, E. A. Mallmann, and L. A. Fricke, “Modelagem de um Conversor CC-CC Ponte Completa Aplicado a Processos de Soldagem a Arco Elétrico,” in *Proc. Seminar on Power Electronics and Control*, pp. 1-6, 2024, doi: 10.53316/sepoc2024.006.

[16] A. D. Tipi, “The Study on the Drop Detachment for Automatic Pipeline GMAW System: short-circuit mode,” *International Journal of Advanced Manufacturing Technology*, vol. 50, pp. 149-161, May 2010, doi: 10.1007/s00170-010-2690-7.

[17] L. Y. H. Meneses, A. M. A. Silva and S. C. A. Alfaro, “Modeling and simulation of the metal transfer on GMAW-S process,” *Journal of the Brazilian Society of Mechanical Sciences and Engineering*, vol. 41, no. 12, pp. 1-18, Nov. 2019, doi: 10.1007/s40430-019-2033-z.

[18] M. K. Bera, “Modeling Simulation of Hybrid Model for the Short-Circuit Mode of Transfer in GMAW Systems,” in *Proc. International Conference on Intelligent Autonomous Systems*, pp. 165-169, 2018, doi: 10.1109/ICoIAS.2018.8493645.

[19] Y. Wang, X. Liu, and H. Jing, “Dynamic simulation of short-circuiting transfer in GMAW based on the ‘mass-spring’ model,” *International journal of Advanced Manufacturing Technology*, pp. 897-907, Oct. 2016, doi: 10.1007/s00170-016-8538-z.

[20] M. Zeng, J. Huang, Y. Zhang, and P. Hu, "Modeling for GMAW process with a current waveform control method," *Journal of Materials Processing Technology*, vol. 240, pp. 404-413, Feb. 2017, doi: 10.1016/j.jmatprotec.2016.10.018.

[21] M. N. O. Sadiku, "Elements of Electromagnetics," 5th ed. Oxford University Press, 2010. ISBN: 978-0195387759.

[22] STMicroelectronics, "STM32F446xC/E Datasheet," Jan. 2021. [Online]. Available: https://www.st.com/resource/en/datasheet/stm32f446mc.pdf

[23] B. Andres, L. C. Bach, M. L. S. Martins, H. L. Hey, and R. C. Beltrame, "Modelling of a ZVS Full-Bridge DC-DC Converter for Photovoltaic Applications," in *Proc. Brazilian Power Electronics Conference*, pp. 1-6, 2017, doi: 10.1109/COBEP.2017.8257323.

[24] R. W. Erickson, and D. Maksimovic, "Fundamentals of Power Electronics," 2nd ed. Norwell: Kluwer Academic Publishers, pp. 213-226, 2001, ISBN: 978-0-306-48048-5.

[25] A. S. Hodel and C. E. Hall, "Variable-structure PID control to prevent integrator windup," IEEE Transactions on Industrial Electronics, vol. 48, no. 2, pp. 442-451, Apr. 2001, doi: https://doi.org/10.1109/41.915424.

BIOGRAPHIES

Christian G. Barbosa was born in Ijuí, Brazil, in 1996, he received the B.S. degree in Electrical Engineering from the Northwest Regional University of the State of Rio Grande do Sul (UNIJUÍ), Brazil, in 2019, and the M.S. degree in Electrical Engineering from the Federal University of Santa Maria (UFSM), Santa Maria, Brazil, in 2023. He is currently pursuing the Ph.D. degree in Electrical Engineering at UFSM. Since 2017, he has been conducting research and development activities related to innovative welding equipment as a member of the R&D team at Balmer – Fricke Soldas. His research interests include control applied to power electronics, industrial automation, embedded systems and control systems, welding processes, and technological innovations in welding.

Vitor de S. Guedes was born in Santa Maria, Brazil, in 2000. He is currently pursuing the B.S. degree in Control and Automation Engineering at the Federal University of Santa Maria (UFSM), Santa Maria, Brazil. Since 2023, he has been a member of the Power Electronics and Control Research Group (GEPOC) at UFSM. He is involved in an extracurricular research and development project focused on the modeling, analysis, and implementation of digital control systems for power electronic converters. His areas of interest include control applied to power electronics, industrial automation, embedded systems and instrumentation.

Rafael C. Beltrame was born in Santa Maria, Brazil, in 1984. He received the B.S., M.S., and Ph.D. degrees in electrical engineering from the Federal University of Santa Maria, Santa Maria, Brazil, in 2008, 2009, and 2012, respectively. He has been with the Power Electronics and Control Research Group (GEPOC) at UFSM since 2005. Since 2013, he has been affiliated with UFSM, where he currently holds a position as a Professor. From 2015 to 2021, he served as the Manager of the High-Voltage Laboratory at the Smart Grids Institute of UFSM. His research interests include high-performance power converters, control applied to power electronics, fast chargers for electric vehicles, and testing of electric power transformers.

Lucas V. Bellinaso received his B.S., M.Sc. and Ph.D. degrees in electrical engineering from the Federal University of Santa Maria (UFSM), in 2012, 2014 and 2017, respectively. Since 2015, he has been with the Power Electronics and Control Group, where he is currently Professor. His research interests include PV systems, power electronics and control applied to renewable energy systems, and safety of PV systems. Additionally, he is currently National Secretary of ABNT/CB-003/CE 003 082, the Brazilian mirror committee of IEC TC 82.

Fábio E. Bisogno received the B.S. and M.S. degrees in Electrical Engineering from the Federal University of Santa Maria (UFSM), Santa Maria, Brazil, in 1999 and 2001, respectively, and the Dr.-Ing. degree in Electrical Engineering from the Technische Universität Chemnitz, Chemnitz, Germany, in 2006. During his doctoral studies, he worked as a Research Engineer at the Fraunhofer Institutes for Autonomous Intelligent Systems (AIS), Reliability and Microintegration (IZM), and later at the Institute for Artificial Intelligence (IAIS), Germany, participating in the conception, design, and development of industrial products for leading companies. From 2009 to 2023, he served as an Associate Professor at UFSM, contributing to the CAPES level-7 graduate program and leading R&D projects in collaboration with electric utilities and industry, with a strong focus on innovation. He is currently a Professor of Electronics in Germany, at the University of Applied Sciences Koblenz (Hochschule Koblenz). His research interests include resonant converters, electronic ballasts, self-oscillating systems lighting systems, and power generation systems using internal combustion engines.

Ezequiel A. Mallmann was born in Mondaí, Santa Catarina, Brazil, in 1987, he received the B.S. degree in Electrical Engineering from the Northwest Regional University of the State of Rio Grande do Sul (UNIJUÍ), Brazil, in 2014. Since 2008, he has in charge of research and development department, developing activities related to innovative welding equipment as a manager of the R&D team at Balmer – Fricke Soldas. His research interests include control applied to power electronics, industrial automation, embedded systems and control systems, welding processes, and technological innovations in welding.

Luciano A. Fricke received the B.S. degrees in electrical engineering from the Federal University of Santa Maria, Santa Maria, Brazil, in 2004. He is currently the Industrial Director and Technical Manager of Fricke Soldas LTDA. He is also the coordinator of the company's research, development and innovation center and coordinator of technological innovation projects in cooperation with companies from Germany, Italy and China.